PAPER

Check for updates

Chemically stable new MAX phase V$_2$SnC: a damage and radiation tolerant TBC material

M. A. Hadi, [ID] *[a] M. Dahlqvist, [ID] [b] S.-R. G. Christopoulos,[c] S. H. Naqib, [ID] [a] A. Chroneos[cd] and A. K. M. A. Islam[ae]

Using density functional theory, the phase stability and physical properties, including structural, electronic, mechanical, thermal and vibrational with defect processes, of a newly synthesized 211 MAX phase V$_2$SnC are investigated for the first time. The obtained results are compared with those found in the literature for other existing M$_2$SnC (M = Ti, Zr, Hf, Nb, and Lu) phases. The formation of V$_2$SnC is exothermic and this compound is intrinsically stable in agreement with the experiment. V$_2$SnC has potential to be etched into 2D MXene. The new phase V$_2$SnC and existing phase Nb$_2$SnC are damage tolerant. V$_2$SnC is elastically more anisotropic than Ti$_2$SnC and less than the other M$_2$SnC phases. The electronic band structure and Fermi surface of V$_2$SnC indicate the possibility of occurrence of its superconductivity. V$_2$SnC is expected to be a promising TBC material like Lu$_2$SnC. The radiation tolerance in V$_2$SnC is better than that in Lu$_2$SnC.

1. Introduction

MAX phases are a family of more than 80 ternary carbides, nitrides and borides in hexagonal crystal symmetry.[1,2] This family is chemically represented as M$_{n+1}$AX$_n$, where M is an early transition metal, A is an A-group element, X is C or N or B, and the integer 'n' ranges from 1 to 3.[3] Depending on the value of layer index n, MAX phases are categorized as 211, 312 and 413 phases for n = 1, 2, 3, respectively. MAX phases crystallize in the hexagonal space group P6$_3$/mmc (194). In their crystal structures, M$_6$X-octahedra with the X-elements fill the octahedral positions between the M-elements as do in the corresponding MX binaries. The octahedra exchange with the A-atomic layers placed at the centers of trigonal prisms, which are larger, and thus more accommodating of the larger A-atoms. The interposing pure metallic A-atomic planes are mirror planes to the meandering ceramic M$_{n+1}$X$_n$ slabs. Due to alternating metallic and ceramic layers in MAX phases they possess a unique set of metallic and ceramic properties.[4] The common metallic properties are electrical and thermal conductivities, high fracture toughness, machinability, damage tolerant and thermal shock resistance. The typical ceramic properties are lightweight, oxidation and corrosion resistance, elastic stiffness, resistant to fatigue and ability to

maintain the strength to high temperature.[5] The MAX phases also experience plastic-to-brittle transitions at high temperatures, and can resist high compressive stresses at ambient temperature.[6] These exceptional properties of MAX phases make them suitable for potential uses as tough and machinable, coatings for electrical contacts, thermal shock refractories, and heating elements at high temperature. Additionally, their neutron irradiation resistance makes them suitable in nuclear applications. A common recent use of MAX phases is as precursors for producing two-dimensional MXenes.[7] The MAX phases are attractive due to their unique combination of structural characteristics, wide range of properties, and many prospective uses.

Early studies on M$_2$SnC phases by Jeitschko *et al.* in mid 1960s resulted in synthesized phases with M = Ti, Zr, Hf, and Nb.[8–10] Kuchida *et al.*[11] synthesized the first Lu-based MAX phase Lu$_2$SnC in the M$_2$SnC family. Lu is the last element in the lanthanide series although it is sometimes mentioned as the first member in the 6th-period transition metals. Lu replaced the common early transition metals "M" in the M$_2$SnC MAX phases. Theoretical investigations reveal that Lu$_2$SnC is softer and more easily machinable than the other existing M$_2$SnC phases. It is also a promising candidate as a thermal barrier coating (TBC) material owing to its high thermal shock resistance, low minimum thermal conductivity, high melting temperature and characteristically good oxidation resistance.[12] Xu *et al.*[13] focused their attention on M$_2$SnC phases and synthesized V$_2$SnC by sintering V, Sn, and C powder mixture at 1000 °C. They identified the crystal structure of V$_2$SnC as 211 MAX phases through X-ray diffraction, first-principles calculation, and high-resolution transmission scanning electron microscopy.

[a]Department of Physics, University of Rajshahi, Rajshahi 6205, Bangladesh. E-mail: hadipab@gmail.com

[b]Thin Film Physics Division, Department of Physics (IFM), Linköping University, SE-581 83 Linköping, Sweden

[c]Faculty of Engineering, Environment and Computing, Coventry University, Priory Street, Coventry CV1 5FB, UK

[d]Department of Materials, Imperial College, London SW7 2AZ, UK

[e]Internatial Islamic University Chittagong, Kumira, Chittagong 4318, Bangladesh

M_2SnC compounds show diversity in their properties. Nb_2SnC and Lu_2SnC show superconducting transition, Nb_2SnC has also better radiation tolerance in the M_2SnC family, Hf_2SnC is highly dense, and Zr_2SnC is highly elastically anisotropic in this group.[5,12] Additionally, the lattice constants of Sn-containing 211 MAX phases show an increasing trend with the crystal radius of M-elements.[12] The diverse properties of M_2SnC motivated the use of density functional theory (DFT) calculations to explore the physical properties of V_2SnC and the analysis of the trend of physical properties in M_2SnC MAX phases. In this study, the mechanical, lattice dynamical and thermodynamic phase stability is examined for the new phase V_2SnC. Mechanical behaviors, elastic anisotropy, Debye temperature, melting point, lattice thermal conductivity, minimum thermal conductivity, lattice dynamics and defect processes of V_2SnC are investigated for the first time.

2. Methodology

All calculations are performed with the DFT method as implemented in CASTEP.[14] The non-spin polarized Perdew–Burke–Ernzerhof (PBE) functional within generalized gradient approximation (GGA) is chosen to describe the electronic exchange-correlation potential.[15] Ultra-soft pseudo-potential developed by Vanderbilt is used to model the interactions between electrons and ion cores.[16] A Γ-centered k-point mesh of $15 \times 15 \times 3$ grid in the Monkhorst-Pack (MP) scheme is used to integrate over the first Brillouin zone in the reciprocal space of the MAX phase hexagonal unit cell.[17] To expand the eigenfunctions of the valence and closely valence electrons in terms of a plane-wave basis, a cutoff energy of 700 eV is chosen. Total energy and internal forces are minimized during the geometry optimization with the BFGS minimization technique named after by the first letter of the name of Broyden–Fletcher–Goldfarb–Shanno.[18] The self-consistence convergence is achieved with the difference in the total energy within 5×10^{-6} eV per atom, the maximum ionic Hellmann–Feynman force within 0.01 eV Å^{-1}, maximum ionic displacement within 5×10^{-4} Å, and maximum stress within 0.02 GPa. For self-consistent field calculations, the tolerance is chosen as 5×10^{-7} eV per atom.

The elastic stiffness constants and moduli are calculated from the first-principles investigations using finite-strain method implemented in the CASTEP code.[19] This method involves setting the deformation to a predetermined value, relaxing all free parameters and computing the stress. The convergence criteria for elastic calculations are chosen as: the difference in total energy within 10^{-6} eV per atom, the maximum ionic Hellmann–Feynman force within 2×10^{-3} eV Å^{-1}, and the maximum ionic displacement within 10^{-4} Å. Elastic calculations with CASEP code have been successful for all kind of crystal systems.[20–31] The lattice dynamic properties such as phonon dispersion and phonon density of states are calculated by means of the finite displacement supercell method executed with a $3 \times 3 \times 1$ supercell within the code.

Defect calculations are performed with a 72-atomic site (36M, 18A, and 18C) supercell using a $3 \times 3 \times 1$ MP k-mesh under constant pressure. Allowing for all possible interstitial sites, an intensive computational search is carried out to identify the potential interstitial sites. The defect energies are defined as effectively energy differences between the isolated defects.

3. Results and discussion

3.1. Structural aspects and phase stability

The newly synthesized V_2SnC phase crystalizes in the hexagonal MAX phase crystal structure with space group $P6_3/mmc$ (no. 194). The position of each atom is found as V at 4f (1/3, 2/3, 0.0744), Sn at 2d (2/3, 1/3, 1/4), and C at 2a (0, 0, 0). The V and Sn atoms stack along the z-direction (c-axis) (see Fig. 1, where M represents V, A refers to Sn and X is C). There are two layers of V atoms in each V–C slab, and every two layers of V atoms and one layer of Sn atoms are consecutively arranged along the z-direction. The optimized lattice constants a and c and internal parameter z_M are in agreement with the experimental and theoretical values.[13] The present values ($a = 3.121$ Å, $c = 12.947$ Å, $z_M = 0.0759$) are closer to the experimental results ($a = 2.981$ Å, $c = 13.470$ Å, $z_M = 0.0776$) compared with the previous theoretical values ($a = 3.134$ Å, $c = 12.943$ Å, $z_M = 0.0751$). The reason may be the use of coarse k-point mesh ($9 \times 9 \times 2$) and low cutoff energy (400 eV) in the previous theoretical study. In the M_2SnC systems, we observed that the unit cell parameters show a better relationship with the crystal radius of M atoms.[12] In this relation, the lattice parameters exhibit increasing trend with the increase of crystal radius of transition metal M. The newly synthesized V_2SnC also obeys this relationship (refer to Fig. 2) (Table 1).

Phase stability of MAX phases with respect to the constituent elements cannot be used to predict whether a material is thermodynamically stable. Instead, all competing phases need to be included in the analysis. The thermodynamic stability of the recently synthesized V_2SnC MAX phase is examined at 0 K with respect to decomposition into any combination of competing phases. The most competitive set of competing phases, designated as equilibrium simplex, is identified using a linear optimization procedure.[34] This procedure has already been
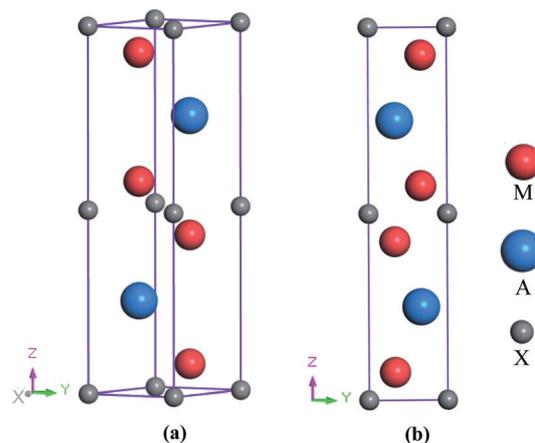

Fig. 1 (a) Crystal structure and (b) 2D view in yz-plane of 211 MAX phase.
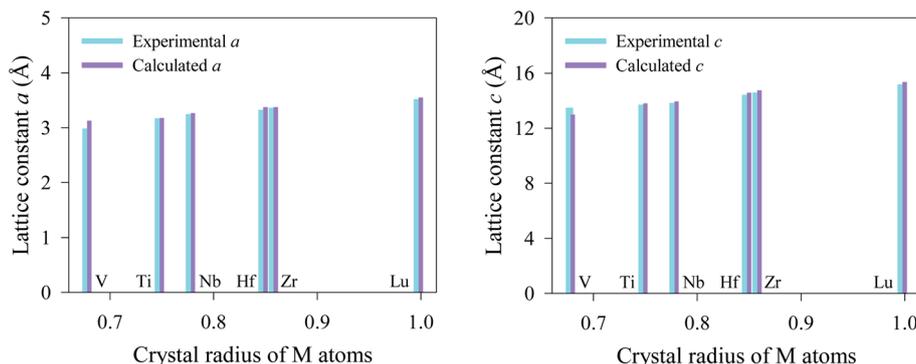
Fig. 2 Lattice parameters of M_2SnC as a function of crystal radius of M atoms.[33]

Table 1 Lattice parameters (a, c, z_M in Å), hexagonal ratio (c/a) and cell volume (V in Å³) of M_2SnC

Compound	a	c	c/a	z_M	V	Remarks
V_2SnC	3.121	12.947	4.148	0.0759	109.2	Calc. (This work)
	2.9792	13.4441	4.513	0.0744	103.3	Expt.[13]
Ti_2SnC	3.172	13.772	4.342	0.0806	120.0	Calc.[12]
	3.1635	13.675	4.323	—	118.5	Expt.[32]
Nb_2SnC	3.258	13.918	4.272	0.0820	128.0	Calc.[12]
	3.2408	13.802	4.259	—	125.5	Expt.[32]
Hf_2SnC	3.367	14.548	4.320	0.0865	142.9	Calc.[12]
	3.3199	14.388	4.334	—	137.3	Expt.[32]
Zr_2SnC	3.367	14.730	4.374	0.0849	144.7	Calc.[12]
	3.3576	14.568	4.339	—	142.2	Expt.[32]
Lu_2SnC	3.546	15.323	4.320	0.0850	166.9	Calc.[12]
	3.514	15.159	4.314	—	162.1	Expt.[32]

successful to confirm the experimentally known MAX phases in addition to predicting the existence of new ones.[35] The stability of V_2SnC is quantified in terms of formation enthalpy ΔH_{cp} by comparing its energy to the energy of the equilibrium simplex according to

$$\Delta H_{cp} = E(V_2SnC) - E(\text{equilibrium simplex}) \quad (1)$$

The phase V_2SnC is considered to be stable if $\Delta H_{cp} < 0$. The considered competing phases for V_2SnC are listed in Table 2. V_2C and Sn are identified as the most competing phases according to linear optimization procedure. The eqn (1) can be rewritten as

$$\Delta H_{cp} = E(V_2SnC) - E(V_2C) - E(Sn) \quad (2)$$

where $E(V_2SnC)$, $E(V_2C)$, and $E(Sn)$ are the ground state total energies of V_2SnC, V_2C and Sn, respectively. Using eqn (2), we find $\Delta H_{cp} = -7$ meV per atom. The negative value of ΔH_{cp} is indicative of the chemical (thermodynamic) phase stability of V_2SnC. In the next Sections 3.2 and 3.5, we will find that V_2SnC is mechanically and dynamically stable compound as well.

3.2. Elastic properties

Elastic constants estimate the response of the crystalline solids to external stresses and measure the strength of the materials.

Elastic constants also provide a fundamental insight into the nature of bonding character between adjacent atomic planes and the anisotropic character of the bonding and structural stability. They can link between a material's dynamical behaviour and its mechanical and thermal properties. For hexagonal MAX phases, five nonzero independent elastic constants, namely C_{11}, C_{12}, C_{13}, C_{33}, and C_{44} are obtained.[36] Table 3 lists the elastic constants of the newly synthesized V_2SnC calculated at zero pressure and zero temperature along with the values found in literatures for existing M_2SnC phases for comparison. For Ti_2SnC, Nb_2SnC, Hf_2SnC, and Zr_2SnC, we have listed C_{ij} calculated with either different codes or different functionals. The CASTEP-GGA results are consistent to the VASP-GGA values. Fig. 3a presents C_{ij} calculated with CASTEP-GGA, in which the M-elements are shown along the x-axis according to the order of their groups for seeking a trend. All C_{ij} show a tendency of monotonic increase when the M-element moves from left to right across the group-3 to −5, though C_{13} shows almost linear increase. The constant C_{66} is not independent as $C_{66} = (C_{11} - C_{12})/2$. The elastic constants of M_2SnC including newly synthesized V_2SnC fulfills the mechanical stability criteria for hexagonal crystals:[37]

$$C_{11}, C_{33}, C_{44} > 0; \ C_{11} > |C_{12}| \text{ and } (C_{11} + C_{12})C_{33} > 2C_{13}C_{13} \quad (3)$$

Furthermore, for all M_2SnC phases, it is observed that the principal elastic constants C_{11} and C_{33} are larger than all other C_{ij}. While for the three systems with M = V, Lu, or Zr, the principal elastic constants are classified as $C_{33} > C_{11}$, and the remaining three systems with M = Hf, Ti, or Nb, exhibit $C_{11} > C_{22}$ within the same code and functional (CASTEP-GGA). It implies that the former group is more incompressible along the c-axis. Either $C_{11} > C_{33}$ or $C_{33} > C_{11}$ is the evident of elastic anisotropy of M_2SnC MAX phases. The phases Ti_2SnC, Zr_2SnC and Lu_2SnC are elastically less anisotropic than other phases as their C_{11} and C_{33} values are very close to each other. The shear elastic constants C_{12} and C_{13} lead mutually to a functional stress component in the crystallographic a-axis with a uniaxial strain along the crystallographic b- and c-axis, respectively. This stress component measures the resistance of shear deformation of a material along the crystallographic b- and c-axis, when stress

Table 2 Lattice parameters, unit cell volume and total energies of V_2SnC and its competing phases

Phase	Prototype structure	Pearson symbol	Space group	a (Å)	b (Å)	c (Å)	V (Å^3)	E (eV fu^{-1})
C	C (graphite)	hP4	$P6_3/mmc$ (194)	2.462744	2.462744	8.985673	47.2	−155.088
C	Diamond	cF8	$Fd\bar{3}m$ (227)	3.567776	3.567776	3.567776	45.4	−154.901
V	W	cI2	$Im\bar{3}m$ (229)	3.011843	3.011843	3.011843	27.3	−1976.398
α-Sn	Diamond	cF8	$Fd\bar{3}m$ (227)	8.596983	8.596983	8.596983	635.4	−94.217
β-Sn	**β-Sn**	**tI4**	**$I4_1/amd$ (141)**	**5.973130**	**5.973130**	**3.183849**	**113.6**	**−95.465**
SnC	ZnS	cF8	$F\bar{4}3m$ (216)	5.134950	5.134950	5.134950	135.4	−248.722
SnC	NaCl	cF8	$Fm\bar{3}m$ (225)	4.921133	4.921133	4.921133	119.2	−247.793
VC	CrB	oC8	$Cmcm$ (63)	2.784524	7.500027	3.378178	70.5	−2131.336
VC	α-MoB	tI16	$I4_1/amd$ (141)	2.875169	2.875169	19.390061	160.3	−2131.692
V_2C	β-V_2N	hP9	$P\bar{3}1m$ (162)	5.017396	5.017396	4.546570	99.1	−4109.186
V_2C	Inverse CdI_2	hP3	$P\bar{3}m1$ (164)	2.908853	2.908853	4.555253	33.4	−4109.146
α-V_2C	**ζ-Fe_2N ($Fe_2N_{0.94}$)**	**oP12**	**$Pbcn$ (60)**	**4.563895**	**5.751247**	**5.040818**	**132.3**	**−4109.208**
β-V_2C	W_2C	hP3	$P6_3/mmc$ (194)	2.908607	2.908606	4.555192	33.4	−4109.147
β'-V_2C	ε-Fe_2N	hP9	$P\bar{3}m1$ (164)	5.003269	5.003269	4.535382	98.3	−4109.191
VC_2	MoB_2	tR18	$R\bar{3}m$ (166)	2.599774	2.599774	24.095326	141.0	−2285.036
VC_2	AlB_2	hP3	$P6/mmm$ (191)	2.554138	2.554138	4.407399	24.9	−2284.212
VC_3	Ni_3Ti	hP16	$P6_3/mmc$ (194)	4.471182	4.471182	7.239285	125.3	−2439.254
V_6C_5	V_6C_5	hP33	$P3_112$ (151)	5.122689	5.122689	14.387631	327.0	−12639.362
V_8C_7		cP60	$P4_332$ (212)	8.328377	8.328377	8.328377	577.7	−16905.598
VSn_2	Mg_2Cu	cF48	$Fddd$ (70)	5.523603	9.500626	18.914470	992.6	−2167.631
V_3Sn	Cr_3Si	cP8	$Pm\bar{3}n$ (223)	5.003758	5.003758	5.003758	125.3	−6024.943
V_3Sn	Mg_3Cd	hP6	$P6_3/mmc$ (194)	5.664976	5.664976	4.517371	125.5	−6025.165
V_3Sn_2	Cr_3Si_2	tP10	$P4/mbm$ (127)	7.107742	7.107742	3.555283	179.6	−6118.656
VSnC	MoAlB	oC12	$Cmcm$ (63)	2.966421	22.230689	2.858936	188.5	−2226.001
V_2SnC	**Cr_2AlC**	**hP8**	**$P6_3/mmc$ (194)**	**3.136333**	**3.136333**	**13.011838**	**110.8**	**−4204.700**
V_2Sn_2C	Mo_2Ga_2C	hP10	$P6_3/mmc$ (194)	3.185703	3.185703	18.846330	165.6	−4299.833
V_3SnC	$CaTiO_3$	cP5	$Pm\bar{3}m$ (221)	4.081427	4.081427	4.081427	68.0	−6180.677
V_3SnC_2	Ti_3SiC_2	hP12	$P6_3/mmc$ (194)	3.055478	3.055478	18.163485	146.9	−6336.856
V_4SnC_3	Ta_4AlN_3	hP16	$P6_3/mmc$ (194)	3.009399	3.009399	23.156747	181.6	−8469.124

is applied along the a-axis. The phase Nb_2SnC is most capable to resist such deformation, while Lu_2SnC will deform easily under the same stress along the a-axis. The new compound V_2SnC is the next most capable phase to resist the deformation in M_2SnC systems if a rank is made one obtains: $Nb_2SnC > V_2SnC > Hf_2SnC > Ti_2SnC > Zr_2SnC > Lu_2SnC$.

Table 3 Elastic properties of M_2SnC (M = V, Ti, Zr, Nb and Hf) MAX phases

Phases	C_{11}	C_{33}	C_{44}	C_{66}	C_{12}	C_{13}	B	G	E	ν	B/G	Remarks
V_2SnC	243	300	87	84	76	124	156	82	209	0.276	1.91	CASTEP-GGA (This work)
	336	304	85	105	126	122	190	95	244	0.286	2.00	CASTEP-GGA[13]
Lu_2SnC	172	173	56	64	46	36	82	61	147	0.199	1.33	CASTEP-GGA[12]
Ti_2SnC	268	265	100	95	79	74	139	97	236	0.217	1.43	CASTEP-GGA[12]
	253	254	93	79	91	74	138	87	217	0.238	1.57	VASP-GGA[46]
	337	329	169	126	86	102	176	138	329	0.188	1.27	FP-L/APW + lo[47]
	303	308	121	109	84	88	160	114	275	0.212	1.40	CASTEP-LDA[48]
							152	83.9	207.4	0.24		Experimental[39,41]
Zr_2SnC	230	232	94	84	62	91	131	83	206	0.237	1.57	CASTEP-GGA[12]
	225	227	87	77	72	90	131	78	196	0.251	1.68	VASP-GGA[46]
	269	290	148	94	81	107	157	110	268	0.215	1.42	FP-L/APW + lo[47]
	279	272	111	104	70	89	147	104	252	0.215	1.42	CASTEP-LDA[48]
								178				Experimental[39]
Hf_2SnC	251	238	101	90	71	107	145	87	218	0.250	1.67	CASTEP-GGA[12]
	249	252	99	85	73	101	144	87	218	0.247	1.65	VASP-GGA[46]
	330	292	167	138	54	126	173	132	316	0.195	1.30	FP-L/APW + lo[47]
	311	306	119	109	92	97	167	112	275	0.225	1.49	CASTEP-LDA[48]
							169		237			Experimental[40]
Nb_2SnC	255	236	94	77	102	122	160	78	202	0.290	2.05	CASTEP-GGA[12]
	253	250	98	74	103	120	160	80	206	0.286	2.00	VASP-GGA[46]
	341	321	183	118	106	169	209	126	315	0.250	1.67	FP-L/APW + lo[47]
	315	309	124	108	99	141	189	107	189	0.262	1.77	CASTEP-LDA[48]
							180		216			Experimental[40]

We have obtained the bulk modulus B and shear modulus G of polycrystalline aggregates from individual elastic constants, C_{ij} by the Hill approximations as implemented within the code.[38] Using B and G, the average Young's modulus E and the Poisson ratio ν can be obtained:

$$E = \frac{9BG}{3B + G} \tag{4}$$

and

$$\nu = \frac{3B - 2G}{6B + 2G} \tag{5}$$

All the elastic moduli B, G, and E and Poisson's ratio ν are also listed in Table 3, from which we observe that the results obtained with the CASTEP-GGA and VASP-GGA are consistent to each other, while the other results deviate considerably. Fig. 3b presents elastic moduli calculated with the CASTEP-GGA scheme. B is highly correlated to the chemical composition and structure, while G is linked to chemical bonding. On the other hand, E measures the response under uniaxial tension averaged over all directions. Within the results of this scheme, B is highest for Nb_2SnC (160 GPa) and lowest for Lu_2SnC (82 GPa). The new phase V_2SnC has second highest value of 156 GPa. Ti_2SnC has highest G (97 GPa) and E (236 GPa) values. The lowest values of G (61 GPa) and E (147 GPa) are found for Lu_2SnC. The new phase V_2SnC has an intermediate value of G (80 GPa) and E (209 GPa). When we move from left to right in the Fig. 3b, we cross the group-3 element (Lu) to group-5 elements (V, Nb) via the group-4 elements (Ti, Zr, Hf). The elastic moduli G and E show the almost similar trend. B of the phases containing groups 3 and 4 elements as M-atom show the similar trend of G and E but the phases containing the group-5 elements show the reverse trend. For comparison, we have found 152 ± 3, 180 ± 5, and 169 ± 4 GPa as the measured values of B for Ti_2SnC, Nb_2SnC, and Hf_2SnC, respectively.[39,40] These values are larger than the values calculated with GGA within CASTEP and VASP codes by 9–14% and smaller than the other values by 2–16%. The experimental shear modulus is found for Ti_2SnC, which is comparable with the GGA-value and much smaller than the other theoretical values listed in Table 3.[41] The experimental Poisson's ratio for Ti_2SnC is 0.24, which is also very close to the GGA-values rather than other values.[41] The experimental value of E for Ti_2SnC, Nb_2SnC, Zr_2SnC, and

Hf_2SnC are 207.4, 216, 178, and 237 GPa, respectively.[40,41] For Nb_2SnC and Hf_2SnC, the experimental E is larger than the theoretical E calculated with both the CASTEP-GGA and VASP-GGA by 7–8%, while the experiment E of Ti_2SnC and Zr_2SnC is smaller than the theoretical E derived with GGA within CASTEP and VASP codes by 5–16%. From other theoretical values listed in Table 3, the experimental E deviates within 13–51%. Therefore, the GGA values of B and E obtained with the CASTEP and VASP codes deviates from experimental values within a reasonable range. The larger the E value, the stiffer the system, and therefore the larger the exfoliation energy.[42] Amongst the productively etched MAX phases into two-dimensional (2D) MXenes, V_2AlC has the largest theoretical exfoliation energy, whose E is reported 311 and 316 GPa.[43,44] Accordingly, the exfoliation energy of new MAX phase V_2SnC and previously observed M_2SnC have lower exfoliation energy than V_2AlC. It is evident that all M_2SnC (M = V, Ti, Zr, Hf, Nb, and Lu) phases have potential to etch into 2D MXenes.

Poisson's ratio ν provides the information regarding the bonding forces and reflects the stability of a material against shear. The M_2SnC MAX phases including newly synthesized V_2SnC have Poisson's ratio within 0.195–0.290. As the obtained values with CASTEP-GGA for V_2SnC, Hf_2SnC and Nb_2SnC fall in the range of 0.25–0.5; their interatomic forces can be considered as central forces.[45] Literature values of ν for Hf_2SnC[46–48] lie on the lower side of this range, while a literature value for Zr_2SnC[46] falls within this range. The values outside this range indicate that the interatomic force is non-central. The low value of ν for Lu_2SnC indicates that it is more stable against shear than other M_2SnC phases including the new phase V_2SnC.[1] Additionally, a pure covalent crystal has a Poisson's ratio of 0.1 and a totally metallic compound has a value of 0.33. As the Poisson's ratio for M_2SnC MAX phases lies between these two characteristic values their atomic bonding is expected to be a mixture of covalent and metallic in nature. Furthermore, Poisson's ratio can classify the solid materials as either brittle or ductile with a value of 0.26.[49,50] Brittle materials have values less than 0.26 and ductile materials have values larger than this value. Accordingly, the new phase V_2SnC and Nb_2SnC are ductile and the remaining phases are brittle. Therefore, V_2SnC and Nb_2SnC are predicted to be damage tolerant.

Bulk modulus to shear modulus ratio (B/G), known as Pugh's ratio can serve as a tool for measuring the ductile/brittle nature
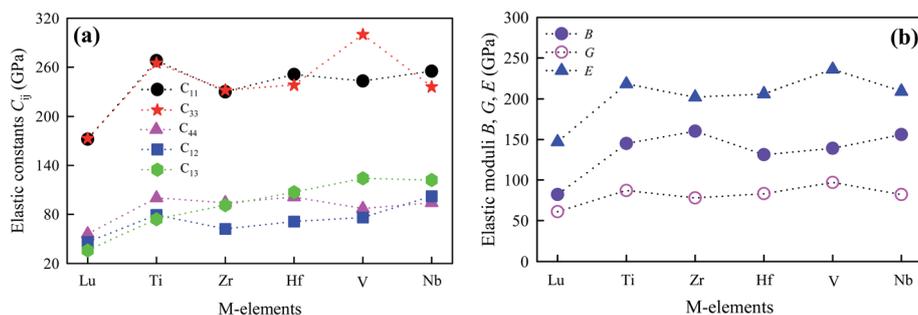

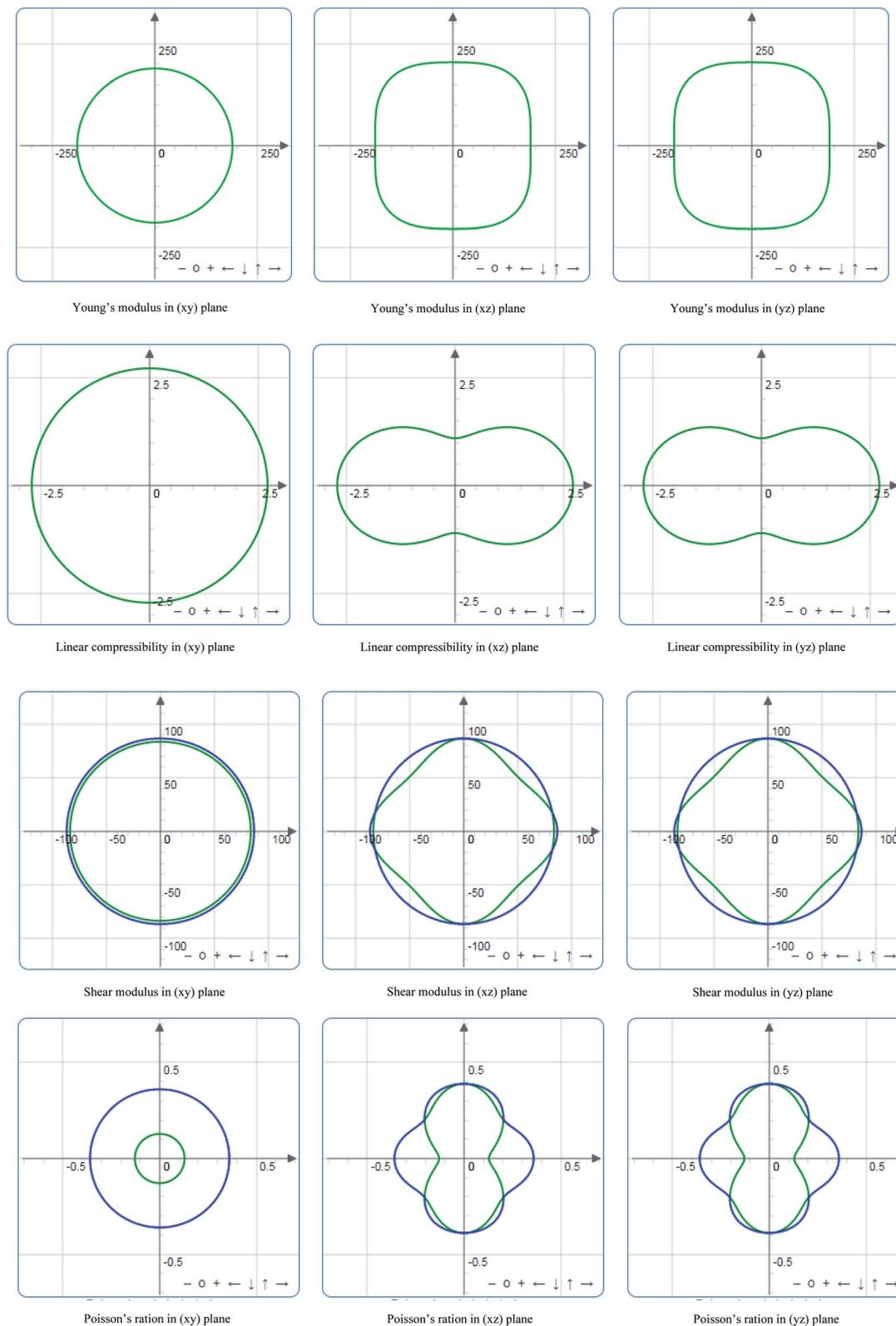**Fig. 3** Elastic constants and moduli of M_2SnC as a function of M-elements.

Fig. 4 Directional dependence of Young's modulus (E), linear compressibility (β), shear modulus (G) and Poisson's ratio (ν) of V_2SnC.

of a material.[51] If the Pugh's ratio is greater than 1.75 the material is expected to be ductile, otherwise it is brittle in nature. Accordingly, V_2SnC and Nb_2SnC are ductile in nature as predicted from their Poisson's ratio.

Indeed, it is essential to analyze and visualize the directional dependence of elastic properties – such as Young's modulus (E), linear compressibility (β), shear modulus (G) and Poisson's ratio (ν) of anisotropic materials – rather than their averages.

For the M_2SnC phases, the directional dependency of E, β, G and ν are calculated using the ELATE suit program[52] and the 2D presentations are shown in Fig. 4 for V_2SnC, indicating that there is no directional dependence in the xy plane as the plots are uniformly circular but in both xz and yz planes there are directional dependences and which are similar in nature as the hexagonal crystal symmetry of V_2SnC. The linear compressibility for some compounds can be negative in some directions, which is represented with an additional curve of red color. For V_2SnC, no negative value is found for any direction. The shear modulus G and Poisson's ratio ν are not so straightforward to represent, as they depend on two orthogonal unit vectors **a** and **b**, which respectively represent the direction of the stress applied and the direction of measurement. For G and ν there are two curves: translucent blue curve represents the maximal values and green curve represents the minimal positive values. There are a lot of compounds having negative Poisson's ratio in some directions. In this case, an additional curve of translucent red represents the negative values. For V_2SnC, no negative Poisson's ratio is found for any directions. For other M_2SnC phases, the above discussions are applicable. The directional dependence of E, β, G and ν in xz and yz planes is almost identical for Nb_2SnC, Hf_2SnC and Zr_2SnC. Ti_2SnC shows almost isotropic nature of E, β, G and ν in xz and yz planes also. The directional dependence of E, β, G and ν in Lu_2SnC is different compared to other M_2SnC phases. Linear compressibility in Ti_2SnC and Lu_2SnC is almost directional independent.

ELATE also provides a quantitative analysis by reporting the minimal and maximal values of each modulus as well as the directions along which these extrema occur. This allows the determination of directions of particular interest in the elastic properties, which are not necessarily along the crystallographic axes of the material. Minimal and maximal values of each

modulus are listed in Table 4. A measure of the anisotropy A_X of each elastic modulus X is defined as follows:

$$A_X = \begin{cases} X_{max}/X_{min} & \text{if } \text{sign}(X_{max}) = \text{sign}(X_{min}) \\ \infty & \text{otherwise} \end{cases} \quad (6)$$

The obtained elastic anisotropy A_X for each elastic modulus is also listed in Table 4. It is observed that Young's modulus shows maximum anisotropy for Nb_2SnC and minimum for Ti_2SnC. Anisotropy in linear compressibility is maximum for V_2SnC and minimum for Ti_2SnC. Anisotropy in shear modulus is highest for Hf_2SnC and lowest for Ti_2SnC. Maximum anisotropy of Poisson's ratio is observed in Hf_2SnC and minimum in Ti_2SnC. Considering all parameters Ti_2SnC is the least anisotropic in M_2SnC family.

Here, we want to quantify the degree of elastic anisotropy of V_2SnC and compare with previously synthesized M_2SnC phases. For hexagonal M_2SnC crystals, there are three shear anisotropy factors linked to C_{ij} that can be determined using the succeeding expressions:[53]

$$A_1 = \frac{(C_{11} + C_{12} + 2C_{33} - 4C_{13})}{6C_{44}}, \quad (7)$$

which is associated with the {100} shear planes between the $\langle 011 \rangle$ and $\langle 010 \rangle$ directions;

$$A_2 = \frac{2C_{44}}{C_{11} - C_{12}}, \quad (8)$$

which is related to the {010} shear planes between the $\langle 101 \rangle$ and $\langle 001 \rangle$ directions; and finally,

$$A_3 = \frac{(C_{11} + C_{12} + 2C_{33} - 4C_{13})}{3(C_{11} - C_{12})}, \quad (9)$$

which signifies shear anisotropy in the {001} shear planes between the $\langle 110 \rangle$ and $\langle 010 \rangle$ directions. For isotropic crystals,

Table 4 Minimal and maximal values of each modulus and elastic anisotropy obtained from them

Phases	Young's modulus (GPa)		Linear compressibility (TPa^{-1})		Shear modulus (GPa)		Poisson's ratio	
	E_{min}	E_{max}	β_{min}	β_{max}	G_{min}	G_{max}	ν_{min}	ν_{max}
V_2SnC	188.79	223.85	1.0964	2.7112	71.355	86.673	0.12849	0.38828
Hf_2SnC	168.97	236.44	1.9579	2.4813	66.846	99.802	0.12198	0.38969
Lu_2SnC	143.59	167.39	3.8307	3.9590	56.841	70.092	0.16641	0.26442
Nb_2SnC	168.47	237.13	1.7785	2.1490	66.303	97.202	0.15262	0.41665
Ti_2SnC	233.72	239.43	2.4154	2.4509	95.408	100.210	0.19446	0.22531
Zr_2SnC	174.63	222.77	2.1404	2.7889	68.418	94.736	0.13615	0.33803

Elastic anisotropy A_X

	A_E	A_β	A_G	A_ν
V_2SnC	1.186	2.4729	1.215	3.0219
Hf_2SnC	1.399	1.2674	1.493	3.1947
Lu_2SnC	1.166	1.0335	1.233	1.5889
Nb_2SnC	1.408	1.2083	1.466	2.7300
Ti_2SnC	1.024	1.0147	1.050	1.1586
Zr_2SnC	1.276	1.3030	1.385	2.4828

Table 5 Elastic anisotropy factors for M_2SnC (M = Lu, Ti, Zr, Hf and Nb) MAX phases

Phases	A_1	A_2	A_3	k_c/k_a	$A_{B\%}$	$A_{G\%}$	A^U	Remarks
V_2SnC	0.8103	1.0419	0.8443	0.4034	1.8476	0.7283	0.1110	CASTEP-GGA (This work)
Lu_2SnC	1.2500	0.8889	1.1111	1.0657	0.0256	0.3781	0.0385	CASTEP-GGA[12]
Ti_2SnC	0.9683	1.0582	1.0247	1.0419	0.0088	0.0284	0.0030	CASTEP-GGA[12]
Zr_2SnC	0.6950	1.1190	0.7778	0.7801	0.2082	0.9355	0.0986	CASTEP-GGA[12]
Hf_2SnC	0.6106	1.1222	0.6852	0.8244	0.1093	1.6814	0.1732	CASTEP-GGA[12]
Nb_2SnC	0.6046	1.2288	0.7429	0.9912	0.0020	1.6962	0.1726	CASTEP-GGA[12]

all A_i's (i = 1, 2, 3) have unit value. A value other than unity quantifies the anisotropic state of crystals. The deviation of A_i from unity (ΔA_i) measures the level of elastic anisotropy in shear.

The calculated values of A_i for V_2SnC are listed in Table 5 along with reported values for other M_2SnC phases and the anisotropy level ΔA_i is shown in Fig. 5, suggesting that all M_2SnC phases including V_2SnC are elastically anisotropic in shear. Shear anisotropy level is highest in Nb_2SnC and lowest in Ti_2SnC in all respects. The anisotropy level in the new phase V_2SnC is higher than that in Ti_2SnC and lower than those in other M_2SnC phases. It is observed that the shear anisotropy level within a group of M atoms of M_2SnC phases increases in the descending order. A different anisotropy factor for hexagonal crystals depending on C_{ij}, i.e. $k_c/k_a = (C_{11} + C_{12} - 2C_{13})/(C_{33} - C_{13})$ is used to quantify the elastic anisotropy upon compression; where k_a and k_c are the linear compressibility coefficients along the a- and c-axis, respectively.[54] Deviation of k_c/k_a from unity ($\Delta(k_c/k_a)$), determines the anisotropy level upon linear compression. The calculated value reveals that the compressibility along the c-axis is smaller than that along the a-axis for the new phase V_2SnC as well as for Zr_2SnC, Hf_2SnC, and Nb_2SnC. For Lu_2SnC and Ti_2SnC the compressibility along the c-axis is greater than that along the a-axis.

According to Hill, the difference between B_V and B_R as well as G_V and G_R is proportional to the degree of elastic anisotropy of crystals, which leads to define the percentage anisotropy factors A_B and A_G with the succeeding equations:[55]

$$A_{B\%} = \frac{B_V - B_R}{B_V + B_R} \times 100\% \qquad (10)$$
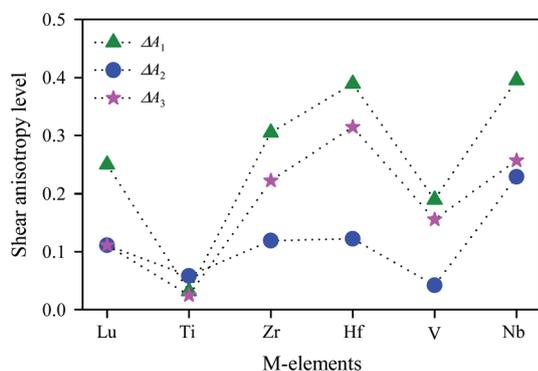
$$A_{G\%} = \frac{G_V - G_R}{G_V + G_R} \times 100\% \qquad (11)$$

The percentage anisotropy factors A_B and A_G calculated for V_2SnC are also listed in Table 5 together with the literature value of other M_2SnC phases. These two factors assign zero values for completely isotropic crystals in view of compressibility and shear, respectively. A positive value quantifies the level of anisotropy. It is evident that the new phase V_2SnC is more anisotropic in compression, whereas Nb_2SnC is more anisotropic in shear. Nb_2SnC is less anisotropic in compression and Ti_2SnC is less anisotropic in shear. An anisotropy factor named "universal anisotropy index" is recently proposed for an appropriate universal measure of elastic anisotropy of crystals and defined as:[56]

$$A^U = 5\frac{G_V}{G_R} + \frac{B_V}{B_R} - 6 \geq 0 \qquad (12)$$

This index has either zero or positive value. Zero value signifies the completely isotropic nature and positive value indicates the anisotropy level in elastic properties of crystals. According to this index (see Table 5), the new phase V_2SnC is more anisotropic than Lu_2SnC, Ti_2SnC and Zr_2SnC and less anisotropic than Hf_2SnC and Nb_2SnC. It is evident that the universal anisotropy level follows the trend of shear anisotropy level. That is, the universal anisotropy level within a group of M atoms of M_2SnC phases increases in the descending order.

3.3. Electronic properties

Electronic structure plays a significant role in understanding of material properties at the microscopic level. Electronic energy band structure calculated along high symmetry points of the Brillouin zone for V_2SnC is shown in Fig. 6a. Similar to other M_2SnC and remaining MAX phases, the band structure of V_2SnC reveals the metallic characteristics as a large number of its valence bands cross the Fermi level E_F and overlap with the conduction bands. The position of Fermi level in V_2SnC is just below the valence band maximum near the Γ-point as in Ti_2SnC.[5] In Nb_2SnC, the Fermi level is above the valence band maximum at the Γ-point.[5] The Γ-point, where the maximum of the valence bands accumulate, lies above the Fermi levels of Sn-based other MAX phases Hf_2SnC, Zr_2SnC and Lu_2SnC (see Fig. 6 in ref. 5). The band structure of V_2SnC is very similar to that of

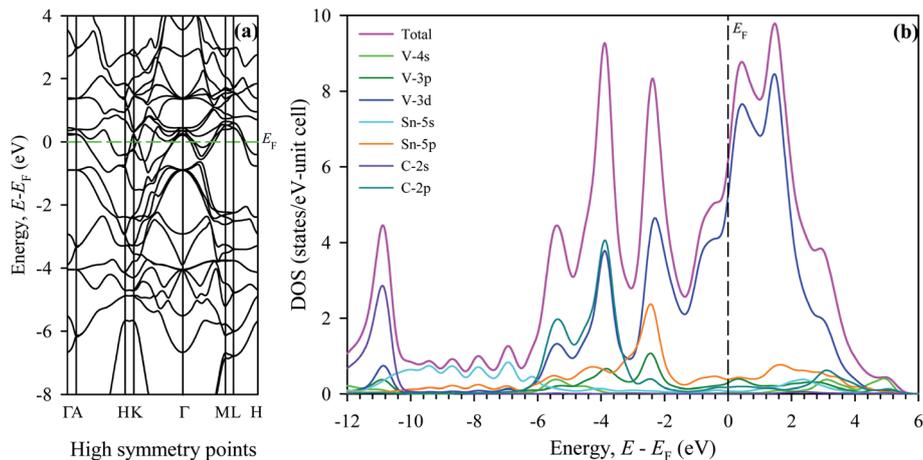**Fig. 5** Shear anisotropy level in M_2SnC MAX phases.

Fig. 6 Electronic structures of V_2SnC, (a) band structure and (b) density of states; E_F denotes the Fermi level.

Nb_2SnC rather than other M_2SnC phases.[5] Nb_2SnC is a super-conducting phase. Resemblance of two band structures indicates the possibility of superconductivity in V_2SnC. The main characteristic of the band structure is the significantly anisotropic nature with less energy dispersion along the c-axis. It is evident from the reduced dispersion along the short H–K and M–L directions. The anisotropic band structure near and below the Fermi level implies that the electrical conductivity is also anisotropic for the new MAX phase studied here.

To realize the bonding nature, the total and partial density of states (DOS) are calculated for V_2SnC and presented in Fig. 6b. The Fermi level of V_2SnC lies far from a pseudogap at the left instead of near a pseudogap as found for other existing M_2SnC MAX phases.[5] Consequently, the new phase V_2SnC is not as stable as other M_2SnC phases. In fact, the Fermi level of V_2SnC lies at the wall of a large peak and as a result V_2SnC has a large total DOS of 6.12 states per eV per unit cell at E_F, whereas the total DOS at E_F for other M_2SnC phases ranges from 2.35–3.93 states per eV per unit cell.[5] The valence band of V_2SnC contains two main parts. An intermediate low flat-type valence band arises due to Sn-s orbitals in similar to in other M_2SnC and M_3SnC_2 compounds.[5,27] The lower valence band consists of a single peak arising owing to the hybridization between V-3d and C-2s states, which indicate strong covalent V–C bond in V_2SnC similar to the M–C bonds in M_2SnC. The higher valence band contains three distinct peaks similar to those of Nb_2SnC.[5] The small peak at the left of the higher valence band arises due to the interaction between V-3d and C-2p-orbitals. The middle peak is the highest peak and arises owing to the hybridization between V-3d and C-2p electrons. The third peak corresponds to the interaction between V-3d and Sn-5p states. This interaction results in weaker covalent V–Sn bonding due to closeness of the peak to the Fermi level. It is clear that the V–C bond is stronger than V–Sn bond as M–C bonds are stronger than M–A bonds. Weaker M–A bond favours the exfoliation of M_2SnC MAX phases to 2D MXenes.[59] The overall bonding nature in the new phase V_2SnC is a combination of metallic, covalent, and, due to the difference in electronegativity between the constituent atoms, ionic like other MAX phase compounds.[1,3,5,27,57]

We have calculated the electron charge density map and Fermi surface to understand the nature of chemical bonding in V_2SnC. In the contour map of electron charge density (Fig. 7a) it is seen that the charge distributions around V atoms are practically spherical and its intensity specifies the amount of charge accumulation. The charge accumulated around the V atom is $0.32e$, whereas the charge accumulation around the M atoms in other M_2SnC systems ranges from 0.28–0.45e.[5] The highest charge is deposited around the Lu atom ($0.45e$) and lowest charge around the Hf atom ($028e$). The V-charge overlaps with the C-charge and slightly edges with the Sn-charge, which indicates the strong V–C and weak V–Sn bonds, respectively. Analogous bonds are also seen in the contour maps of other M_2SnC compounds.[5] The spherical charge distributions around the atoms also indicate some ionic nature in chemical bonds in V_2SnC as well as in other M_2SnC MAX phases.

The Fermi surface (FS) calculated for the V_2SnC MAX phase is shown in Fig. 7b, which contains four different sheets. All sheets are seen to be centered along the Γ–A direction. The first and second sheets are cylindrical. They have an extra part like a half-folded plain sheet along each L–M direction. The third sheet shows a lot of nesting nature. It has also an additional
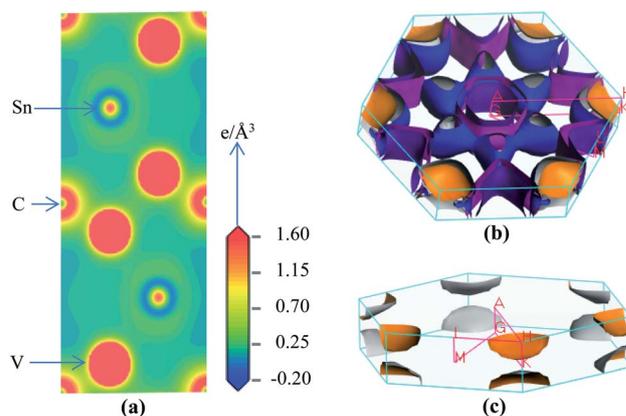

Fig. 7 Electronic structures of V_2SnC; (a) charge density map, (b) Fermi surface and (c) fourth Fermi sheet.

part along H–K directions, whose shape is like a cylinder cutting parallel to its axis. The fourth sheet consists of two identical parts along the H–K directions. The lower part is just the mirror inversion of the upper part (Fig. 7c). As seen from Fig. 5a, near the Γ (0,0,0) point, two hole-like bands appear, giving rise to two hole-like Fermi surface sheets near the Γ point (first and second sheets). Conversely, the calculated band structure near the H(1/3, 1/3, 1/3) point consists of two electron-like bands, corresponding to two electron-like Fermi surface sheets near the H point (third and fourth sheets). The FS of V_2SnC has a lot of similarities to that of superconducting Nb_2SnC among all M_2SnC MAX phases.[5] Nb_2SnC is a superconducting phase having nesting nature in its FS. This nesting plays a role in strong electron–phonon interactions and is ultimately able to enhance the superconducting order of the material.[58] Nesting nature is an indication of superconductivity of V_2SnC. We hope that the experimentalists will be stimulated to confirm the prediction.

3.4. Thermal properties

In this section, we have reported the elastic Debye temperature, melting point, lattice thermal conductivity and minimum thermal conductivity of V_2SnC. Debye temperature θ_D is a characteristic temperature of solid materials that can be calculated from the elastic moduli using Anderson method.[59] This method is simple and rigorous, which determines θ_D using average sound velocity calculated from the shear and bulk moduli *via* the equation:

$$\theta_D = \frac{\hbar}{k_B}\left[\left(\frac{3n}{4\pi}\right)\frac{N_A\rho}{M}\right]^{1/3} v_m. \tag{13}$$

In this equation, $\hbar$ and k_B are respectively the Plank and Boltzmann constants, N_A is Avogadro's number, ρ is the mass density, n is the number of atoms in a molecule, and M is the molecular weight. The average sound velocity v_m is obtained from the longitudinal and transverse sound velocities v_l and v_t by the equation:

$$v_m = \left[\frac{1}{3}\left(\frac{1}{v_l^3}+\frac{2}{v_t^3}\right)\right]^{-1/3}. \tag{14}$$

With the bulk modulus B and shear modulus G, v_l and v_t can be determined as:

$$v_l\left(\frac{3B+4G}{3\rho}\right)^{1/2} \text{ and } v_t = \left(\frac{G}{\rho}\right)^{1/2}. \tag{15}$$

The obtained sound velocities and Debye temperature of V_2SnC is listed in Table 6 along with the literature values for existing M_2SnC phases and the CASTEP-GGA values are given in Fig. 8. There are several sets of literature values of θ_D for M = Ti, Zr, Hf, and Nb. It is observed that the values derived with the GGA functional using the CASTEP and VASP codes are consistent as we have a close measured value (380 K) and a theoretical value (412 K) of θ_D for Nb_2SnC.[60,61] The remaining two sets of θ_D values show large deviations from the former sets as well as from the available experimental and theoretical values. It is evident from the Fig. 8 that the sound velocities and Debye temperature follow the reverse trend of shear and universal anisotropy level. That is, the sound velocities and Debye temperature within a group of M atoms of M_2SnC phases decrease in the descending order.

The Debye temperatures of M_2SnC MAX phases follow the order of $Lu_2SnC < Hf_2SnC < Nb_2SnC < Zr_2SnC < V_2SnC < Ti_2SnC$. High average sound velocity corresponds to a high Debye

Table 6 Sound velocities in km s^{-1}, Debye temperature and melting point in K, minimum and lattice thermal conductivity in W m^{-1} K^{-1} of M_2SnC (M = Lu, Ti, Zr, Hf and Nb) MAX phases

Phases	ρ	v_l	v_t	v_m	θ_D	T_m	κ_{min}	κ_{ph}[b]	Remarks
V_2SnC	7.073	6.125	3.405	3.792	472	1533	1.20	14.38	CASTEP-GGA (This work)
Lu_2SnC	9.847	4.073	2.489	2.748	300	1130	0.51	14.91	CASTEP-GGA[12]
Ti_2SnC	6.346	6.503	3.910	4.325	525	1556	0.99	29.98	CASTEP-GGA[12]
	6.346	6.327	3.703	4.106	498	1494	1.23	22.24	VASP-GGA[46,a]
	6.473	7.113	4.337	4.790	585	1859	1.45	49.51	FP-L/APW + lo[47]
	6.76	6.783	4.099	4.532	561	1725	1.08	36.87	CASTEP-LDA[48]
Zr_2SnC	7.313	5.749	3.369	3.735	426	1392	0.76	20.61	CASTEP-GGA[12]
	7.313	5.669	3.266	3.627	414	1370	0.73	17.22	VASP-GGA[46,a]
	7.280	6.357	3.831	4.236	483	1596	0.86	34.67	FP-L/APW + lo[47]
	7.75	6.111	3.683	4.073	472	1599	0.86	31.82	CASTEP-LDA[48]
Hf_2SnC	11.796	4.704	2.716	3.015	348	1464	0.63	15.92	CASTEP-GGA[12]
	11.796	4.695	2.716	3.015	348	1479	0.63	16.15	VASP-GGA[46,a]
	11.828	5.228	3.118	3.446	398	1782	0.72	32.92	FP-L/APW + lo[47]
	12.06	5.121	3.050	3.376	393	1746	0.71	26.94	CASTEP-LDA[48]
Nb_2SnC	8.369	5.616	3.053	3.469	412	1473	0.76	12.38	CASTEP-GGA[12]
	8.369	5.645	3.092	3.448	410	1488	0.76	12.61	VASP-GGA[46,a]
	8.388	6.358	3.626	4.030	480	1859	0.89	29.96	FP-L/APW + lo[47]
	8.53	6.150	3.493	3.883	469	1763	0.87	22.92	CASTEP-LDA[48]

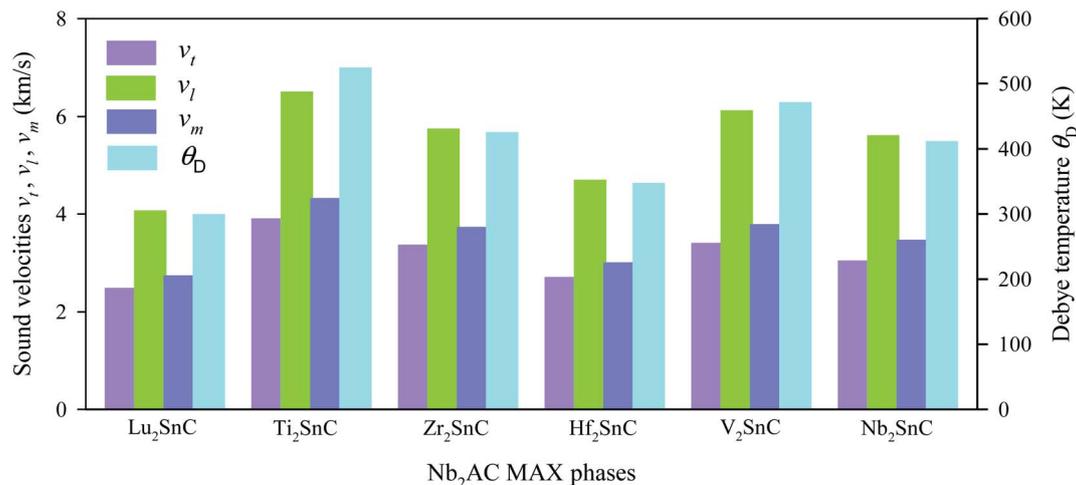[a] Calculated from published data. [b] Calculated at 300 K.

Fig. 8 Elastic sound velocities and Debye temperature of M_2SnC phases.

temperature of Ti_2SnC. The new phase V_2SnC has the second highest Debye temperature. Lu_2SnC has a low Debye temperature because of its low average sound velocity. Generally, the higher the Debye temperature the stiffer the material. Therefore, V_2SnC is softer than Ti_2SnC and stiffer than the other existing M_2SnC MAX phases. A low Debye temperature results in low thermal conductivity of a material, which favors it for being a promising thermal barrier coating (TBC) material.[62] The Debye temperature of a promising TBC material, $Y_4Al_2O_9$ is 564 K,[63] which is larger than those of existing M_2SnC phases. Therefore, M_2SnC phases including new phase V_2SnC have possibility to be potential TBC materials if they have low thermal conductivity, high thermal expansion coefficient, high melting point and oxidation resistance. For comparison, we have experimental Debye temperature only for Nb_2SnC (380 K),[60] which is comparable to the theoretical value (412 K).[13]

Lattice thermal conductivity is one of the most fundamental properties of solids. As the MAX phases have dual characters of metals and ceramics, therefore, to determine their lattice thermal conductivity, the Slack model is appropriate as it deals with materials having partial ceramic nature.[64] The model considers the average of the atoms (M/n) in a "molecule" (or the atoms in the formula unit of the crystal) and their average atomic weight. This model is useful to determine the temperature-dependent lattice thermal conductivity of materials. On the other hand, Clarke's model is very advantageous for calculating the temperature-independent minimum thermal conductivity of compounds.[1] Slack's equation for calculating the lattice thermal conductivity is

$$\kappa_{ph} = A \frac{M_{av}\theta_D^3\delta}{\gamma^2 n^{2/3} T} \tag{16}$$

In this formulation, M_{av} is the average atomic mass in kg mol^{-1}, θ_D is the Debye temperature in K, δ is the cubic root of average atomic volume in m, n is the number of atoms in a conventional unit cell, T is the temperature in K, and γ is the

Grüneisen parameter, which is calculated from the Poisson's ratio with the equation

$$\gamma = \frac{3(1+\nu)}{2(2-3\nu)}. \tag{17}$$

The factor $A(\gamma)$ due to Julian[65] can be obtained as

$$A(\gamma) = \frac{5.720 \times 10^7 \times 0.849}{2 \times (1 - 0.514/\gamma + 0.228/\gamma^2)}. \tag{18}$$

The lattice thermal conductivity of V_2SnC calculated at room temperature (300 K) is listed in Table 6 and its temperature dependence is shown in Fig. 9. Table 5 also lists the literature values for other existing M_2SnC phases. Lattice thermal conductivity is highly sensitive to the Debye temperature. As the
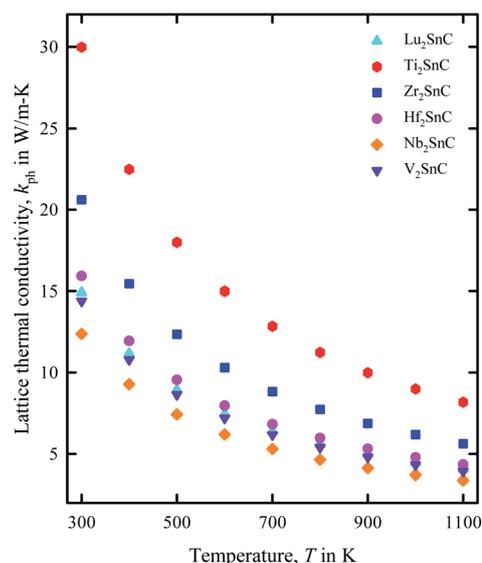

Fig. 9 Variation of lattice thermal conductivity of M_2SnC phases with temperature T.

Debye temperature agrees fairly with the experimental value for the theoretical results with the GGA functional within the CASTEP and VASP codes, the room temperature lattice thermal conductivity calculated with the same functional within the same codes is expected to be consistent with the experiment if it is done in future. The reliability of Slack model has been established for MAX phases as their calculated lattice thermal conductivity agrees fairly well with the experimental values. For instance, the calculated (experimental) lattice thermal conductivity at 1300 K for Ta_4AlC_3 and Nb_4AlC_3 are 5 (6) W m^{-1} K^{-1} and 7 (7) W m^{-1} K^{-1}, respectively.[61] The lattice thermal conductivity at room temperature for M_2SnC MAX phases ranges from 14 to 30 W m^{-1} K^{-1} within the CASTEP-GGA calculations, which does not exceed the typical range for MAX phases.[66] Fig. 9 exhibits the gradual decrease of lattice thermal conductivity of M_2SnC with the increase of temperature. The new phase V_2SnC has lattice thermal conductivities very close to those of Lu_2SnC for the whole range of temperatures. Lu_2SnC is already predicted as better TBC materials among M_2SnC (M = Lu, Ti, Nb, Zr, Hf) phases.[12] Therefore, the new phase V_2SnC is expected to be a promising TBC material as Lu_2SnC.

The theoretical lower limit of intrinsic thermal conductivity of a material at high temperature is defined as its minimum thermal conductivity. The phonons become unpaired at high temperature and hence the heat energy is transferred to the adjacent atoms. In this situation, the mean free path of phonons is supposed to be the average interatomic distance. According to this approximation, different atoms can be substituted within a molecule with an equivalent atom having average atomic mass of M/n (n is the number of atoms in a primitive cell). A single "equivalent atom" within the cell never exhibits optical modes and hence it can be used to derive a formulation to determine the minimum thermal conductivity κ_{min} at high temperature, as Clarke described in his model:[67]

$$\kappa_{min} = k_B v_m \left(\frac{n N_A \rho}{M} \right) \tag{19}$$

The symbols used in this expression carry the same meanings of those used in eqn (4). The minimum thermal conductivity calculated for the new MAX phase V_2SnC is listed in Table 6 along with literature values for other M_2SnC MAX phases. In the similar fashion of other properties, the minimum thermal conductivity calculated with GGA functional within CASTEP and VASP codes show more consistency than other results listed in Table 6. For comparison, we have another theoretical result of 0.755 W m^{-1} K^{-1} for Nb_2SnC,[61] which is identical to 0.76 W m^{-1} K^{-1} obtained in the present and a previous[46] calculations with GGA within CASTEP and VASP codes. The new phase has the highest value of 1.20 W m^{-1} K^{-1} among M_2SnC phases considering same functional within same code, which is very close to 1.13 W m^{-1} K^{-1} of a promising TBC material, $Y_4Al_2O_9$.[63] Additionally, the ultralow minimum thermal conductivity of 1.25 W m^{-1} K^{-1} is used for selecting appropriate materials for TBC applications.[68] Therefore, M_2SnC phases including new phase V_2SnC have the possibility to be promising TBC materials.

3.5. Vibrational properties

To verify the dynamical stability of the newly synthesized V_2SnC MAX phase, the phonon dispersion and phonon density of states are investigated. The phonon dispersion curve is shown in the left panel of Fig. 10. There is no negative phonon frequency in the whole Brillouin zone. The absence of negative phonon frequency ensures the absence of soft phonon modes, indicating that the phase V_2SnC is dynamically stable against the mechanical perturbation at ambient state like the other existing M_2SnC phases.[12] 211 MAX phases have eight atoms in their unit cell, which lead to 24 vibrational modes including three acoustic and 21 optical modes. The lower branches correspond to the acoustic modes (orange) and the upper branches with frequencies greater than 2 THz correspond to the optical modes (light blue). Lower optical branches overlap with the acoustic branches and consequently there is no phononic band gap between the acoustic and optical branches. The zero phonon frequency of the acoustic modes at the Γ point is another indication of dynamical stability of the V_2SnC MAX phase. The phonon DOS shown in the right panel of Fig. 10, reveals that the acoustic and lower optical modes arise due to the vibration of heavier atoms Sn and V. The higher optical
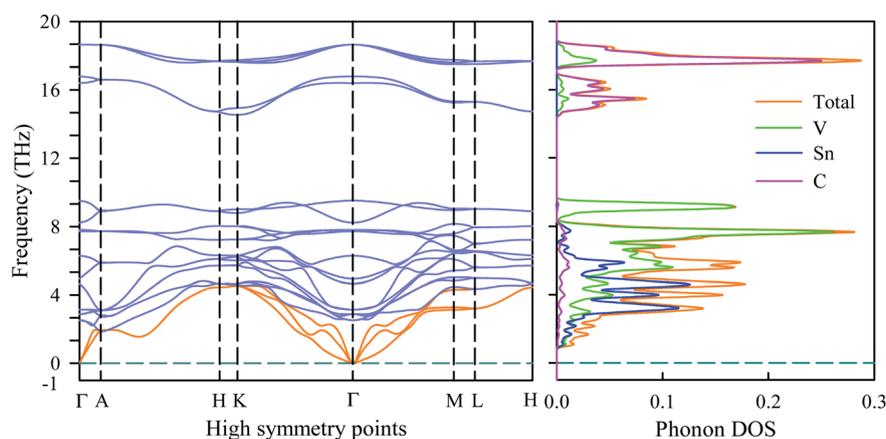

Fig. 10 Phonon dispersion and phonon DOS of V_2SnC.

modes mainly originate from the vibration of lighter atom C. Acoustic phonon is caused by the coherent vibrations of atoms in a lattice outside their equilibrium position. On the other hand, when an atom moves to the left and its neighbour to the right, the optical phonon is originated due to the out-of-phase oscillation of the atom in a lattice. Optical phonons control the most of the optical properties of crystals.

3.6. Vickers' hardness

Herein, the theoretical method based on Mulliken population developed by Gou et al.[69] is used to calculate the Vickers' hardness of partial metallic compounds. Within this method, the bond hardness H_v^μ is calculated as:

$$H_v^\mu = 740\left(P^\mu - P^{\mu'}\right)\left(v_b^\mu\right)^{-5/3} \tag{20}$$

where P^μ is the Mulliken overlap population of the μ-type bond, $P^{\mu'}$ is the metallic population and can be calculated with the unit cell volume V and the number of free electrons in a cell, n_{free} as follows: $n_{\text{free}} = \int_{E_P}^{E_F} N(E)\mathrm{d}E$ and $P^{\mu'} = \dfrac{n_{\text{free}}}{V}$, E_P and E_F are the energy at the pseudogap and at the Fermi level, respectively, v_b^μ is the volume of μ-type bond and is calculated from the bond length d^μ of μ-type and the number of bonds N_b^v of v type per unit volume using the equation $v_b^\mu = (d^\mu)^3/\sum_v[(d^\mu)^3 N_b^v]$. Then, the theoretical Vickers hardness for complex multiband crystal can be determined as a geometric average of all bond hardness values as follows:

$$H_V = \left[\prod^\mu \left(H_v^\mu\right)^{n^\mu}\right]^{1/\sum n^\mu} \tag{21}$$

where n^μ represents the number of μ-type bonds. The Vickers' hardness calculated for M_2SnC including new phase V_2SnC is listed in Table 6. The new phase V_2SnC has highest Vickers' hardness in the M_2SnC family. There are two sets of experimental values for Ti_2SnC, Zr_2SnC, Hf_2SnC, and Nb_2SnC.[32,70] The determined values show deviations from one set to another, except in the case of Ti_2SnC. Indeed, the determined values depend on the purity of the sample, instrumental set up and error. The present theoretical values (refer to Table 7) also differ from the experimental values. The temperature of the sample may be an additional reason. The theoretical H_V of M_2SnC ranges from 0.2 to 2.9 GPa. It is worth mentioning that the measured values of H_V for MAX phases range from 2 to 8 GPa.

The theoretical H_V of Lu_2SnC is very small compared to the lower limit of measured value for MAX phases. The reason may be the absence of typical M–C bond in the structure of Lu_2SnC. This also reduces the elastic constants, elastic moduli and melting and Debye temperature in Lu_2SnC. Consequently, Lu_2SnC is the most soft and easily machinable compound in M_2SnC as well as in MAX family. Indeed, the hardness of MAX phases is very small compared to their corresponding binary phases. Low hardness of MAX phases makes them machinable compounds. All phases in M_2SnC family are easily machinable compared to many other MAX phases.

3.7. Defect processes

Frenkel defect energies provide the information regarding nuclear applications of a material as the low pair formation energy is linked to a higher content of more persistent defects. These in turn cause the loss of ordering in the structure of a crystal. An accumulation of defects in a crystal that are formed by the displacement cascades are indicative of radiation tolerance of the material.[71,72] In Table 8, the relations (1–3) are the key reactions for the Frenkel defects in Kröger–Vink notation[73] for M_2SnC phases.

Antisite defects are point defects formed due to either recombination or occupation of atoms at alternative lattice sites during radiation damage.[71] Low energy antisite formation energy indicates that a major population of residual defects will persist in a material, as a net reduction of defect mobility arises due to change of an interstitial into an antisite.[71,74] The antisite formation mechanisms are given by the reactions (4)–(6) in Table 8.

Displacive radiation causes an athermal concentration of Frenkel pairs, as it is assumed that the radiation tolerance of materials depends on the resistance to form persistent populations of Frenkel (and antisite) defects.[72] In this context, high defect energy is indicative of radiation tolerance. In a previous study of M_2SnC (M = Lu, Ti, Zr, Hf, and Nb) phases, Nb_2SnC is predicted as most radiation tolerant MAX phase in these systems.[5] If the new phase V_2SnC is included in these systems Nb_2SnC remains at the same position. Comparing with other M_2SnC phases, the radiation tolerance in V_2SnC is better than Lu_2SnC and lower than remaining ones.

Although the M interstitials, according to reaction (9), will recombine with V'_{Sn} to form M_A antisites for all the M_2SnC MAX phases studied here, there will be very little concentration of M_i

Table 7 Bond number n^μ, bond length, d^μ (Å), bond population P^μ, bond volume v_b^μ (Å^3), bond hardness H_v^μ (GPa), metallic population $P^{\mu'}$, and hardness H_V (GPa) of M_2SnC MAX phases

Compound	Bond	n^μ	d^μ	P^μ	$P^{\mu'}$	v_b^μ	H_v^μ	H_V	H_V (expt.)
V_2SnC	V–C	4	2.0526	1.02	0.05432	27.30	2.9	2.9	
Ti_2SnC	Ti–C	4	2.1414	1.08	0.01525	30.00	2.7	2.7	3.5,[32] 3.5[70]
Zr_2SnC	Zr–C	4	2.3118	1.05	0.01302	36.18	1.9	1.9	3.5,[32] 3.9[70]
Lu_2SnC	Sn–C	4	4.3478	0.12	0.00348	41.82	0.2	0.2	
Hf_2SnC	Hf–C	4	2.3158	1.39	0.00541	35.73	2.6	2.6	3.8,[32] 4.5[70]
Nb_2SnC	Nb–C	4	2.2014	0.99	0.00139	31.98	2.3	2.3	3.8,[70] 3.5[70]

Table 8　The defect reaction energies as calculated for V_2SnC and existing M_2SnC [5] MAX phases

Reaction (V′ denotes vacancy)	Defect energy (eV)					
	V_2SnC	Lu_2SnC	Ti_2SnC	Zr_2SnC	Hf_2SnC	Nb_2SnC
1　$M_M \rightarrow V'_M + M_i$	6.40	6.61	8.75	8.66	9.34	8.70
2　$Sn_{Sn} \rightarrow V'_{Sn} + Sn_i$	7.95	3.57	8.97	6.63	7.51	7.56
3　$C_C \rightarrow V'_C + C_i$	5.12	2.23	6.10	5.34	4.68	5.18
4　$M_M + Sn_{Sn} \rightarrow M_{Sn} + Sn_M$	4.67	3.67	4.92	4.83	4.72	5.12
5　$M_M + C_C \rightarrow M_C + C_M$	9.37	11.79	12.81	15.40	16.37	12.64
6　$Sn_{Sn} + C_C \rightarrow Sn_C + C_{Sn}$	8.64	7.75	9.98	9.64	10.07	10.05
7　$Sn_i + V'_M \rightarrow Sn_M$	−5.17	−3.61	−6.86	−4.71	−5.17	−4.34
8　$C_i + V'_M \rightarrow C_M$	−0.80	−0.13	−1.07	0.12	1.47	−0.48
9　$M_i + V'_{Sn} \rightarrow M_{Sn}$	−4.51	−2.90	−5.94	−5.75	−6.96	−6.79
10　$C_i + V'_{Sn} \rightarrow C_{Sn}$	0.03	1.56	−0.19	0.22	0.89	−0.10
11　$M_i + V'_C \rightarrow M_C$	−1.35	3.08	−0.97	1.28	0.88	−0.76
12　$Sn_i + V'_C \rightarrow Sn_C$	−4.46	0.39	−4.91	−2.55	−3.01	−2.58
13　$M_i + Sn_{Sn} \rightarrow M_{Sn} + Sn_i$	3.44	0.67	3.03	0.88	0.55	0.76
14　$M_i + C_C \rightarrow M_C + C_i$	3.77	5.31	5.13	6.62	5.56	4.42
15　$Sn_i + M_M \rightarrow Sn_M + M_i$	1.24	3.01	1.89	3.95	4.17	4.36
16　$Sn_i + C_C \rightarrow Sn_C + C_i$	0.66	2.62	1.19	2.79	1.67	2.60
17　$C_i + M_M \rightarrow C_M + M_i$	5.60	6.49	7.69	8.78	10.81	8.22
18　$C_i + Sn_{Sn} \rightarrow X_{Sn} + Sn_i$	7.98	5.13	8.79	6.85	8.40	7.46
Schottky reaction	5.83	9.99	7.97	9.69	8.57	6.70

in the first place due to the very high reaction energies of reaction (1) listed in Table 8. Under equilibrium conditions, this will effectively render reaction (7) practically irrelevant. Similar arguments are also applicable for the other antisite reactions (8) and (9). These reactions may become pertinent in the case of a non-equilibrium environment (*i.e.*, under irradiation) where an increased defect concentration is feasible. In this environment, it is expected that M_i will recombine with V'_{Sn} to produce M_A antisites. Moreover, the creation of C_{Sn} through the reaction (8) should be anticipated for Ti_2SnC. After irradiation, these processes may only be relevant, given that the formation energies of the M_i defects according to the Frenkel reaction (relation-(1)) are high for all the M_2SnC MAX phases studied here (6.40–9.34 eV, refer to Table 8). The processes considered for the displacement of lattice atoms by interstitials (reactions (13)–(18)) are all positive in energy. The new phase requires lowest energy in Schottky reaction. From an experimental point of view, the radiation tolerance and oxidation resistance of M_2SnC phases have to be determined at high temperature. A detailed understanding of the radiation tolerance of V_2SnC requires systematic experimental work and simulation over a range of timescales and system sizes.

4.　Conclusions

In summary, the density functional theory is employed to investigate the phase stability and physical properties of a newly synthesized 211 MAX phase, V_2SnC for the first time. The calculated results are compared with those of other existing M_2SnC (M = Ti, Zr, Hf, Nb, and Lu) phases. The newly synthesized compound V_2SnC has passed the mechanical, dynamic and thermodynamic stability tests. The new phase V_2SnC is the

second most capable phase to resist the deformation in M_2SnC systems following the order: $Nb_2SnC > V_2SnC > Hf_2SnC > Ti_2SnC > Zr_2SnC > Lu_2SnC$. It also has the second highest value of B and θ_D and an intermediate value of G and E in the M_2SnC family. V_2SnC is softer than Ti_2SnC and stiffer than other existing M_2SnC MAX phases. V_2SnC has potential to be etched into 2D MXene like the other M_2SnC phases. V_2SnC and Nb_2SnC are ductile and damage tolerant and the remaining phases are brittle in nature. The directional dependence of E, β, G and ν of M_2SnC is calculated. All M_2SnC phases show directional dependence of E, G, and ν in the xz and yz planes. Ti_2SnC and Lu_2SnC show almost directional independency on β. Elastic anisotropy in V_2SnC is higher than Ti_2SnC and less than the other M_2SnC phases. The band structure and Fermi surface are indicative of possible superconductivity of V_2SnC. V_2SnC is anticipated to be a promising TBC material as Lu_2SnC among M_2SnC phases. V_2SnC is more radiation tolerant than Lu_2SnC and less than the remaining other M_2SnC phases.

Authors contribution

M. A. Hadi: conceptualization, data curation, investigation, methodology, formal analysis, writing – original draft. M. Dahlqvist: software, formal analysis, review & editing; S.-R. G. Christopoulos: investigation, data curation; S. H. Naqib: project administration, review & editing; A. Chroneos: formal analysis, writing, review & editing. A. K. M. A. Islam: formal analysis, review & editing.

Data availability

Supplementary data will be made available on request.

Conflicts of interest

There are no conflicts of interest to declare.

References

1 M. A. Hadi, *J. Phys. Chem. Solids*, 2020, **138**, 109275.
2 T. Rackl, L. Eisenburger, R. Niklaus and D. Johrendt, *Phys. Rev. Mater.*, 2019, **3**, 054001.
3 M. W. Barsoum, *Prog. Solid State Chem.*, 2000, **28**, 201–281.
4 D. Horlait, S. Grasso, A. Chroneos and W. E. Lee, *Mater. Res. Lett.*, 2016, **4**, 137–144.
5 M. A. Hadi, N. Kelaidis, S. H. Naqib, A. Chroneos and A. K. M. A. Islam, *Comput. Mater. Sci.*, 2019, **168**, 203–212.
6 D. J. Tallman, E. N. Hoffman, E. N. Caspi, B. L. Garcia-Diaz, G. Kohse, R. L. Sindelar and M. W. Barsoum, *Acta Mater.*, 2015, **85**, 132–143.
7 M. A. Hadi, M. A. Rayhan, S. H. Naqib, A. Chroneos and A. K. M. A. Islam, *Comput. Mater. Sci.*, 2019, **170**, 109144.
8 H. Nowotny and F. Benesovsky, *J. Less-Common Met.*, 1964, **7**, 133–138.
9 W. Jeitschko and H. N. F. Benesovsky, *Monatsh. Chem.*, 1963, **94**, 1198–1200.
10 F. Benesovsky, *Monatsh. Chem.*, 1963, **94**, 332–333.
11 S. Kuchida, T. Muranaka, K. Kawashima, K. Inoue, M. Yoshikawa and J. Akimitsu, *Physica C Supercond.*, 2013, **494**, 77–79.
12 M. A. Hadi, N. Kelaidis, S. H. Naqib, A. Chroneos and A. K. M. A. Islam, *J. Phys. Chem. Solids*, 2019, **129**, 162–171.
13 Q. Xu, Y. Zhou, A. Jiang, H. Zhang, Q. Tao, J. Lu, J. Rosen, S. Grasso and C. Hu, *J. Adv. Ceram.*, 2020, **9**, 481–492.
14 S. J. Clark, M. D. Segall, C. J. Pickard, P. J. Hasnip, M. I. J. Probert, K. Refson and M. C. Payne, *Z. Kristallogr.*, 2005, **220**, 567.
15 J. P. Perdew, K. Burke and M. Ernzerhof, *Phys. Rev. Lett.*, 1996, **77**, 3865.
16 D. Vanderbilt, *Phys. Rev. B: Condens. Matter Mater. Phys.*, 1990, **41**, 7892.
17 H. J. Monkhorst and J. D. Pack, *Phys. Rev. B: Condens. Matter Mater. Phys.*, 1976, **13**, 5188.
18 T. H. Fischer and J. Almlof, *J. Phys. Chem.*, 1992, **96**, 9768.
19 F. D. Murnaghan, *Finite Deformation of an Elastic Solid*, Wiley, New York, 1951.
20 M. A. Hadi, M. T. Nasir, M. Roknuzzaman, M. A. Rayhan, S. H. Naqib and A. K. M. A. Islam, *Phys. Status Solidi B*, 2016, **253**, 2020–2026.
21 M. A. Hadi, M. Roknuzzaman, A. Chroneos, S. H. Naqib, A. K. M. A. Islam, R. V. Vovk and K. Ostrikov, *Comput. Mater. Sci.*, 2017, **137**, 318–326.
22 M. H. K. Rubel, M. A. Hadi, M. M. Rahaman, M. S. Ali, M. Aftabuzzaman, R. Parvin, A. K. M. A. Islam and N. Kumada, *Comput. Mater. Sci.*, 2017, **138**, 160–165.
23 M. Roknuzzaman, M. A. Hadi, M. A. Ali, M. M. Hossain, N. Jahan, M. M. Uddin, J. A. Alarco and K. Ostrikov, *J. Alloys Compd.*, 2017, **727**, 616–626.
24 M. T. Nasir, M. A. Hadi, M. A. Rayhan, M. A. Ali, M. M. Hossain, M. Roknuzzaman, S. H. Naqib,

25 A. K. M. A. Islam, M. M. Uddin and K. Ostrikov, *Phys. Status Solidi B*, 2017, **254**, 1700336.
25 S.-R. G. Christopoulos, P. P. Filippatos, M. A. Hadi, N. Kelaidis, M. E. Fitzpatrick and A. Chroneos, *J. Appl. Phys.*, 2018, **123**, 025103.
26 A. M. M. Tanveer Karim, M. A. Hadi, M. A. Alam, F. Parvin, S. H. Naqib and A. K. M. A. Islam, *J. Phys. Chem. Solids*, 2018, **117**, 139–147.
27 M. A. Hadi, S.-R. G. Christopoulos, S. H. Naqib, A. Chroneos, M. E. Fitzpatrick and A. K. M. A. Islam, *J. Alloys Compd.*, 2018, **748**, 804–813.
28 M. A. Hadi, M. N. Islam and M. H. Babu, *Z. Naturforsch., A: Phys. Sci.*, 2019, **74**, 71.
29 P. P. Filippatos, M. A. Hadi, S.-R. G. Christopoulos, A. Kordatos, N. Kelaidis, M. E. Fitzpatrick, M. Vasilopoulou and A. Chroneos, *Materials*, 2019, **12**, 4098.
30 M. N. Islam, M. A. Hadi and J. Podder, *AIP Adv.*, 2019, **9**, 125321.
31 M. Mozahar Ali, M. A. Hadi, M. L. Rahman, F. H. Haque, A. F. M. Y. Haider and M. Aftabuzzaman, *J. Alloys Compd.*, 2020, **821**, 153547.
32 M. W. Barsoum, G. Yaroschuck and S. Tyagi, *Scr. Mater.*, 1997, **37**, 1583–1591.
33 R. D. Shannon, *Acta Crystallogr., Sect. A: Cryst. Phys., Diffr., Theor. Gen. Crystallogr.*, 1976, **32**, 751.
34 M. Dahlqvist, B. Alling, I. A. Abrikosov and J. Rosén, *Phys. Rev. B: Condens. Matter Mater. Phys.*, 2010, **81**, 024111.
35 A. S. Ingason, A. Petruhins, M. Dahlqvist, F. Magnus, A. Mockute, B. Alling, L. Hultman, I. A. Abrikosov, P. O. Å. Persson and J. Rosen, *Mater. Res. Lett.*, 2014, **2**, 89–93.
36 M. A. Hadi, S. H. Naqib, S.-R. G. Christopoulos, A. Chroneos and A. K. M. A. Islam, *J. Alloys Compd.*, 2017, **724**, 1167–1175.
37 M. Born, On the stability of crystal lattices. I, *Mathematical Proceedings of the Cambridge Philosophical Society*, Cambridge University Press, 1940, p. 160.
38 R. Hill, *Proc. Phys. Soc., London, Sect. A*, 1952, **65**, 349.
39 B. Manoun, S. K. Saxena, G. Hug, A. Ganguly, E. N. Hoffman and M. W. Barsoum, *J. Appl. Phys.*, 2007, **101**, 113523.
40 T. El-Raghy, S. Chakraborty and M. W. Barsoum, *J. Eur. Ceram. Soc.*, 2000, **20**, 2619–2625.
41 T. Lapauw, K. Vanmeensel, K. Lambrinou and J. Vleugels, *J. Alloys Compd.*, 2015, **631**, 72–76.
42 A. Champagne, F. Ricci, M. Barbier, T. Ouisse, D. Magnin, S. Ryelandt, T. Pardoen, G. Hautier, M. W. Barsoum and J.-C. Charlier, *Phys. Rev. Mater.*, 2020, **4**, 013604.
43 S. Aryal, R. Sakidja, M. W. Barsoum and W.-Y. Ching, *Phys. Status Solidi B*, 2014, **251**, 1480–1497.
44 M. F. Cover, O. Warschkow, M. M. M. Bilek and D. R. McKenzie, *J. Phys.: Condens. Matter*, 2009, **21**, 305403.
45 M. A. Hadi, *Comput. Mater. Sci.*, 2016, **117**, 422–427.
46 S. Aryal, R. Sakidja, M. W. Barsoum and W.-Y. Ching, *Phys. Status Solidi B*, 2014, **251**, 1480–1497.
47 M. B. Kanoun, S. Goumri-Said and A. H. Reshak, *Comput. Mater. Sci.*, 2009, **47**, 491–500.
48 A. Bouhemadou, *Phys. B*, 2008, **403**, 2707.

49 I. N. Frantsevich, F. F. Voronov and S. A. Bokuta, *Elastic Constants and Elastic Moduli of Metals and Insulators Handbook*, Naukova Dumka, Kiev, 1983, pp. 60–180.

50 G. Vaitheeswaran, V. Kanchana, A. Svane and A. Delin, *J. Phys.: Condens. Matter*, 2007, **19**, 326214.

51 S. F. Pugh, *Philos. Mag.*, 1954, **45**, 823.

52 R. Gaillac, P. Pullumbi and F.-X. Coudert, *J. Phys.: Condens. Matter*, 2016, **28**, 275201.

53 M. A. Ali, M. A. Hadi, M. M. Hossain, S. H. Naqib and A. K. M. A. Islam, *Phys. Status Solidi B*, 2017, **254**, 1700010.

54 M. Roknuzzaman, M. A. Hadi, M. J. Abedin, M. T. Nasir, A. K. M. A. Islam, M. S. Ali, K. Ostrikov and S. H. Naqib, *Comput. Mater. Sci.*, 2016, **113**, 148–153.

55 D. H. Chung and W. R. Buessem, in *Anisotropy in Single Crystal Refractory Compound*, ed. F. W. Vahldiek and S. A. Mersol, vol. 2 Plenum, New York, 1968, p. 217.

56 I. S. Ranganathan and M. Ostoja-Starzewski, *Phys. Rev. Lett.*, 2008, **101**, 055504.

57 M. A. Hadi, U. Monira, A. Chroneos, S. H. Naqib, A. K. M. A. Islam, N. Kelaidis and R. V. Vovk, *J. Phys. Chem. Solids*, 2019, **132**, 38–47.

58 D. Yan, D. Geng, Q. Gao, Z. Cui, C. Yi, Y. Feng, C. Song, H. Luo, M. Yang, M. Arita, S. Kumar, E. F. Schwier, K. Shimada, L. Zhao, K. Wu, H. Weng, L. Chen, X. J. Zhou, Z. Wang, Y. Shi and B. Feng, *Phys. Rev. B*, 2020, **102**, 205117.

59 O. L. Anderson, *J. Phys. Chem. Solids*, 1963, **24**, 909.

60 S. E. Lofland, J. D. Hettinger, T. Meehan, A. Bryan, P. Finkel, S. Gupta, M. W. Barsoum and G. Hug, *Phys. Rev. B: Condens. Matter Mater. Phys.*, 2006, **74**, 174501.

61 C. Dhakal, S. Aryal, R. Sakidja and W.-Y. Ching, *J. Eur. Ceram. Soc.*, 2015, **35**, 3203–3212.

62 D. R. Clarke and S. R. Phillpot, *Mater. Today*, 2005, **8**, 22–29.

63 Y. Zhou, H. Xiang, X. Lu, Z. Feng and Z. Li, *J. Adv. Ceram.*, 2015, **4**, 83–93.

64 D. T. Morelli and G. A. Slack, in *High Thermal Conductivity Materials*, ed. S.L. Shinde and J. S. Goela, Springer, New York, 2006, pp. 37–68.

65 C. L. Julian, *Phys. Rev.*, 1965, **137**, A128.

66 M. W. Barsoum, *MAX Phases: Properties of Machinable Ternary Carbides and Nitrides*, John Wiley & Sons, Weinheim, Germany, 2013.

67 D. R. Clarke, *Surf. Coat. Technol.*, 2003, **163**, 67–74.

68 Y. Liu, V. R. Cooper, B. Wang, H. Xiang, Q. Li, Y. Gao, J. Yang, Y. Zhou and B. Liu, *Mater. Res. Lett.*, 2019, **7**, 145–151.

69 H. Gou, L. Hou, J. Zhang and F. Gao, *Appl. Phys. Lett.*, 2008, **92**, 241901.

70 T. El-Raghy, S. Chakraborty and M. W. Barsoum, *J. Eur. Ceram. Soc.*, 2000, **20**, 2619–2625.

71 S. C. Middleburgh, G. R. Lumpkin and D. Riley, *J. Am. Ceram. Soc.*, 2013, **96**, 3196–3201.

72 K. E. Sickafus, L. Minervini, R. W. Grimes, J. A. Valdez, M. Ishimaru, F. Li, K. J. McClellan and T. Hartmann, *Science*, 2000, **289**, 748–751.

73 F. A. Kröger and H. J. Vink, *Solid State Phys.*, 1956, **3**, 307–435.

74 R. E. Voskoboinikov, G. R. Lumpkin and S. C. Middleburgh, *Intermetallics*, 2013, **32**, 230–232.